

# Improving ultra-fast charging performance and durability of all solid state thin film Li-NMC battery-on-chip systems by *in situ* TEM lamella analysis

León Romano Brandt<sup>a,\*</sup>, Kazunori Nishio<sup>b</sup>, Enrico Salvati<sup>a,c</sup>, Kevin P. Simon<sup>d,1</sup>, Chrysanthi Papadaki<sup>a</sup>, Taro Hitosugi<sup>b</sup>, Alexander M. Korsunsky<sup>a,\*\*</sup>

<sup>a</sup> Korsunsky group, Multi-Beam Laboratory for Engineering Microscopy (MBLEM), Department of Engineering Science, University of Oxford, Parks Road, Oxford OX1 3PJ, United Kingdom

<sup>b</sup> School of Materials and Chemical Technology, Tokyo Institute of Technology, Tokyo 152-8552, Japan

<sup>c</sup> Polytechnic Department of Engineering and Architecture (DPIA), University of Udine, Via delle Scienze 206, Udine, Italy

<sup>d</sup> Department of Mechanical Engineering, Massachusetts Institute of Technology, Cambridge, MA 02139, USA

## ARTICLE INFO

### Article history:

Received 18 August 2021

Revised 7 November 2021

Accepted 17 November 2021

### Keywords:

All solid state batteries  
NMC, thin film  
FIB-DIC, *in situ* charging  
Electron nano-diffraction  
Fast charging  
Modelling

## ABSTRACT

All solid state, thin film Li-NMC batteries produced by Physical Vapour Deposition have the potential to revolutionize the internet of things by integrating ultra-fast charging and high energy densities into small portable devices. In these systems, the integrity of the cathode-solid electrolyte interface is of particular importance, as it determines the internal battery resistance and attainable charge rate. To understand and control the effect of manufacturing parameters on the performance and interface stability in these systems, as well as the mechanisms resulting in interface degradation, a novel approach was used that combined *in situ* battery lamella charging with electron nano-diffraction and multiphysics Finite Element modeling. Experimentally observed cathode strains and degradation were correlated with deposition parameter-controlled grain orientation, to determine ideal deposition conditions for enhanced thin film battery charging and discharging behavior. It was identified that (104) oriented cathode grains minimize anode-electrolyte interface degradation, while allowing for high charge and discharge rates, as well as significantly reducing the cathode-electrolyte interface resistance. Furthermore, the residual stress state of individual thin film battery layers, as well as the cathode grain orientation were identified as material design parameters to optimize cell performance and durability with potential capacity retention enhancements of up to 28%.

© 2021 Elsevier Ltd. All rights reserved.

## 1. Introduction

Rechargeable Li-ion batteries have become indispensable for various aspects of human mobility and connectivity, including electric vehicles, mobile phones and other portable appliances. Driven by the exponential growth of the internet of things (IoT) in the past decade [1], a significant increase in demand for communicating devices without hardwire for either power or communications has emerged. To meet this demand, specialised micro-scale, fast charging, and high-energy Li-ion batteries with carefully de-

signed cathode and electrolyte materials are required, in addition to a highly scalable manufacturing process. In this context, thin film, solid state  $\text{LiNi}_{1/3}\text{Co}_{1/3}\text{Mn}_{1/3}\text{O}_2$  (Li-NMC) batteries with  $\text{Li}_3\text{PO}_4$  electrolyte produced by physical vapor deposition (PVD) can be employed in a wide range of emerging cutting-edge technological applications. These include, amongst others, flexible electronics and wearable medical devices [2–4], as well as autonomous microelectro-mechanical systems (A-MEMS), which find increasing use across biology, medicine, agriculture and environmental monitoring [5]. The key advantage of employing PVD for thin film battery manufacture include the ability to deposit all battery components directly onto a chip, thus enabling precise tailoring of the battery properties and dimensions to match application requirements.

Conventional Li-ion battery technologies with high Cobalt content and liquid electrolyte suffer from comparably low attainable charging rates [6,7], safety risks related to the use of flammable

\* Corresponding author.

\*\* Corresponding author at: University of Oxford, Department of Engineering Science, Parks Road, Oxford, Oxfordshire OX1 3PJ, United Kingdom.

E-mail addresses: [leon.romanobrandt@eng.ox.ac.uk](mailto:leon.romanobrandt@eng.ox.ac.uk) (L. Romano Brandt), [alexander.korsunsky@eng.ox.ac.uk](mailto:alexander.korsunsky@eng.ox.ac.uk) (A.M. Korsunsky).

<sup>1</sup> Department of Materials, University of Oxford, Parks Road, Oxford, OX1 3PH, United Kingdom

liquid electrolytes [8], high raw material cost [9,10], and cycling induced performance degradation [11,12]. Solid state thin film batteries, on the other hand, overcome these challenges thanks to a high level of material design control during manufacturing. This way, they enable extraordinarily high charge rates of more than  $14 \text{ mA cm}^{-2}$  (3600C) [13] thanks to two effects: firstly, the large surface-to-volume ratio present in the multilayer system results in short Lithium diffusion pathways from anode to cathode, making these systems ideal candidates for the use of solid electrolyte due to the limited effects of increased resistance as compared to liquid electrolyte. Commonly used materials for solid electrolytes include  $\text{Li}_3\text{PO}_4$  used in this study, as well as Sulfide electrolytes [14,15]. Secondly, precisely controlled PVD parameters in vacuum permit the creation of a cathode-electrolyte interface with extremely low resistance [13], thus allowing an interface with defined atomic structures. This impurity-free and atomically controlled interface lead to a full charge and discharge cycle at high current density. At the same time, the use of solid state electrolyte increases operational safety by preventing the risk of a thermal runaway [16]. Replacing expensive Co with other transition metals such as Ni and Mn results in so called NMC compositions ( $\text{LiNi}_x\text{Mn}_y\text{Co}_z\text{O}_2$ , where  $x + y + z = 1$ ), which can be synthesised in different compositions (often represented in the form of integer ratios, i.e. NMC111, NMC622, NMC811, etc.), thus enabling substantial cost savings, while unlocking increased energy densities with higher Ni content. Long-term cycling stability was further confirmed for the thin film batteries used in the present study, with very limited capacity loss observed over 100 cycles following an initial significant capacity drop of around 28% after the first cycle [17].

Addressing the cause of this initial capacity drop is fundamental for the further optimization of thin film battery performance and reliability. A key aspect of microstructural control during cathode deposition is the grain orientation, which crucially impacts the  $\text{Li}^+$  ion diffusion direction, strain accommodation, and determines the mechanisms of degradation [11]. Preferential expansion and contraction directions of the hexagonal unit cell during first charge and discharge can result in a significant stress build-up that ultimately leads to battery degradation. In this study, we correlate the cathode microstructural orientation and stress state with strain and fracture observation obtained from *in situ* lamella charging experiments. Supported by finite element simulations, our experimental results give rise to the use of grain orientation selection as a means of strain accommodation and charging performance design.

## 2. Materials and methods

Due to the employed Li thin film as anode top layer, the samples were highly air and moisture sensitive. To prevent performance degradation, the thin film batteries were stored exclusively in Ar atmosphere after deposition. For the transfer between glove box and FIB-SEM instrument, a pressure-sensitive self-sealing transfer module, as shown in Fig. 1 was employed [18]. Based on the motion of a piston with changing pressure differential, the transfer module automatically opens under high vacuum and closes as soon as the pressure in the chamber increases. The SEM chamber was further vented exclusively with Argon to ensure an air and moisture free environment and sample re-usability.

### 2.1. All-in-vacuum deposition

Using the pulsed laser deposition (PLD) technique,  $\text{LiNi}_{1/3}\text{Mn}_{1/3}\text{Co}_{1/3}\text{O}_2$  (NMC) thin films were grown on  $\text{LaNiO}_3(001)$  thin films on  $\text{SrTiO}_3(001)$  substrates. First, the substrate ( $5 \times 5 \text{ cm}^2$  with a thickness of 0.5 mm) was annealed at  $1100^\circ\text{C}$  for 5 min at an oxygen pressure ( $P_{\text{O}_2}$ ) of  $1 \times 10^{-5}$  Torr to prepare

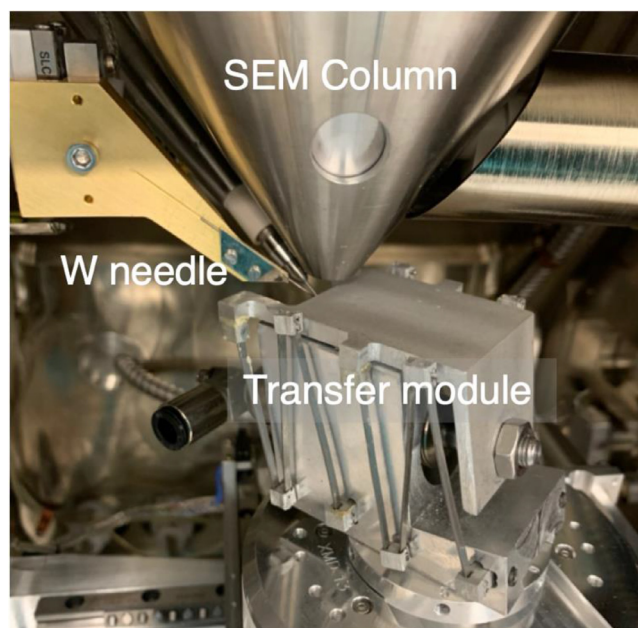
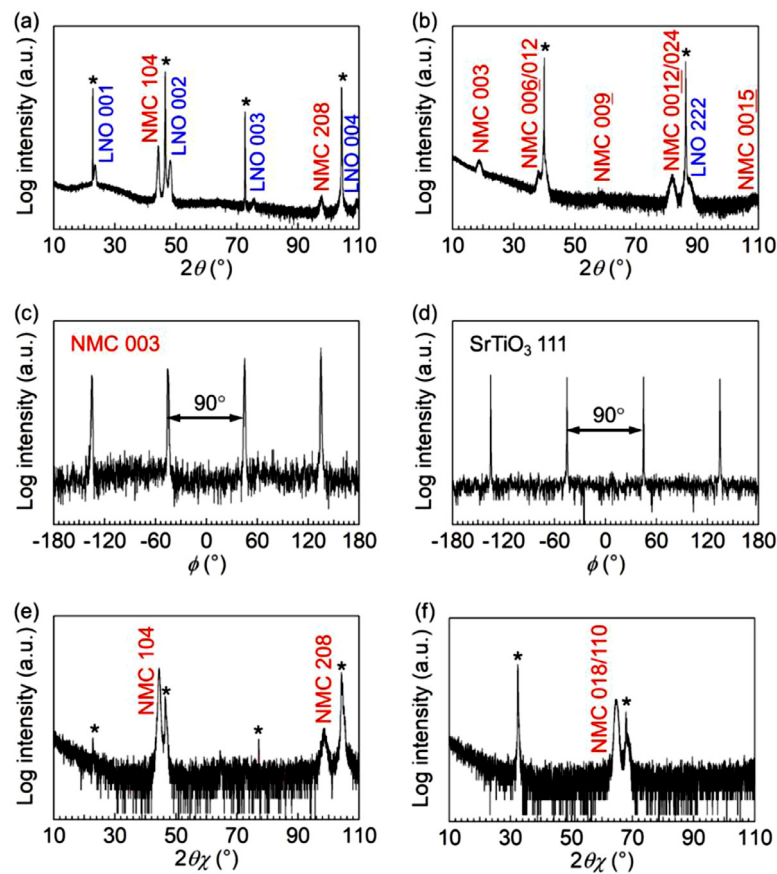


Fig. 1. Self-sealing transfer module for sample transfer between glove box and FIB-SEM instrument inside the vacuum chamber. The shown geometry is used for the lamella lift-out.

a step-terrace surface. Then, a  $\text{LaNiO}_3(001)$  thin film, which was used as a current collector for the thin-film lithium batteries, was grown on the substrate by performing the PLD using a KrF excimer laser (wavelength of 248 nm, pulse duration of approximately 20 ns, laser fluence of  $1.60 \text{ J cm}^{-2}$ , and repetition rate of 2 Hz). A  $\text{LaNiO}_3$  polycrystalline target (Toshiba Manufacturing Co., Ltd.) was used for the target ablation. The substrate temperature ( $T_s$ ) and  $P_{\text{O}_2}$  were set as  $650^\circ\text{C}$  and  $2 \times 10^{-1}$  Torr during the growth. An NMC thin film was deposited on the  $\text{LaNiO}_3$  thin film by performing PLD by using the KrF excimer laser (laser fluence of  $0.7 \text{ J cm}^{-2}$  and repetition rate of 5 Hz). A polycrystalline target of  $\text{Li}_{1.2}\text{Ni}_{1/3}\text{Mn}_{1/3}\text{Co}_{1/3}\text{O}_2$  (TOSHIMA manufacturing Co., Ltd.) was used for the target ablation. The laser intensity at a target was monitored before the growth. The target-substrate distance was approximately 47 mm. For the NMC thin-film growth,  $T_s$  and  $P_{\text{O}_2}$  were set as  $600^\circ\text{C}$  and 100 mTorr, respectively. Extensive X-Ray diffraction sample characterization confirming the substrate-cathode orientation relation was carried out post deposition, as shown in Fig. 2, Fig. 3 respectively, and described in [17].

### 2.2. FIB-SEM lamella sectioning and in situ charging

For the creation of a functioning multilayer lamella micro-battery, transmission electron microscopy (TEM) lamellae were sectioned from the multilayer battery sample using the Focused Ion Beam (FIB) of a Tescan Lyra 3XM instrument at the Multi-Beam Laboratory for Engineering Microscopy (University of Oxford, UK). After depositing a  $1 \mu\text{m}$  thin protective Pt layer on the target area, a low FIB beam current of 11 nA at 30 kV accelerating voltage was chosen to avoid short circuit currents induced by the ion beam. The final dimensions of the obtained lamellae after low current ion beam surface polishing were  $10 \times 7 \times 1 \mu\text{m}^2$ . *In situ* charging was carried out inside the FIB-SEM instrument. For this purpose, the three top layers consisting of anode, solid electrolyte and NMC layer were partially removed to avoid short circuiting during lamella attachment. Subsequently, the substrate and current collector layers were connected to a TEM copper grid using Pt deposition. Finally, the nano-manipulator needle was attached to the protective surface Pt layer in order to establish an electric connec-



**Fig. 2.** X-ray diffraction (XRD) patterns for the  $\text{LiNi}_{1/3}\text{Mn}_{1/3}\text{Co}_{1/3}\text{O}_2$  (NMC) (thickness of 40 nm)/ $\text{LaNiO}_3$  (thickness of 15 nm)/ $\text{SrTiO}_3(001)$  substrate. (a) Out-of-plane XRD pattern. (b) Out-of-plane XRD pattern collected under a skew geometry along the  $\text{SrTiO}_3[111]$  direction. Azimuthal  $\phi$ -scan of the (c) NMC 003 and (d)  $\text{SrTiO}_3$  111 reflections. In-plane XRD patterns along the (e)  $\text{SrTiO}_3[010]$  and (f)  $\text{SrTiO}_3[110]$  directions. The asterisks in the figures indicate the diffractions from the  $\text{SrTiO}_3$  substrate. Adapted from [17].

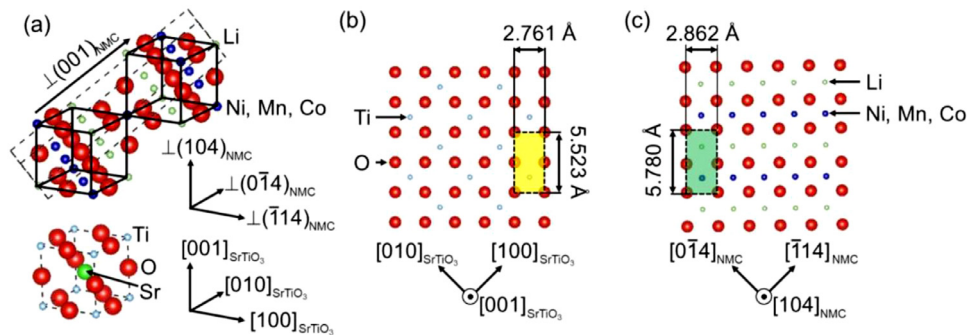


**Fig. 3.** (a) Crystal orientation relationship for  $\text{LiNi}_{1/3}\text{Mn}_{1/3}\text{Co}_{1/3}\text{O}_2$  (NMC)(104) on  $\text{SrTiO}_3(001)$ . Dashed black lines represent unit cells of NMC and  $\text{SrTiO}_3$ . Black lines indicate pseudo-cubic structure in NMC. Schematically illustrated top views of (b)  $\text{TiO}_2$  layer of  $\text{SrTiO}_3$  (001), and (c) NMC(104) plane. Yellow and green squares in (b) and (c) indicate the similarity of the oxygen anion arrangements in  $\text{SrTiO}_3$  and NMC, respectively. Adapted from [17].

tion, as shown in Fig. 8. Due to the beam sensitivity of the samples, imaging was kept to a minimum. A built-in pico-amp potentiostat normally employed for the characterization of semiconductor materials was connected to both ends of the lamella battery and operated in potentiostatic mode. A voltage ramp from 2.5 V to 4.5 V was run for a duration of 120 s. One SEM frame before and after the charge was acquired in order to keep beam-induced damage to a minimum. A MATLAB-based Digital Image Correlation (DIC) software package [19] was used to track surface features on the NMC layer, thus permitting the calculation of x- and y-displacements, based on which horizontal and vertical strains were calculated.

### 2.3. Transmission EDX

Energy-dispersive X-Ray spectroscopy in transmission mode (t-EDX) is a highly effective tool for the elemental sample characterization at high resolution, as the sample-beam interaction is limited to the lamella thickness. To enable nano-resolution analysis, thin, electron-transparent lamellae were sectioned as described in the previous section, but followed by thinning to a final thickness of around 100 nm using low current FIB polishing. T-EDX analysis was carried out at the E01 beamline at Diamond Light Source (Harwell, UK) using a JEOL ARM200CF high resolution scanning transmission electron microscope (STEM) equipped with a JEOL Centurio dual



**Table 1**

Material properties used for the calculation of the residual stress depth profile based on eigenstrain analysis.

Layer	Young's Modulus E [GPa]	Poisson's Ratio
Li [24]	4.9	0.37
Li <sub>3</sub> PO <sub>4</sub> [25–29]	105.9	0.25
LiNi <sub>1/3</sub> Co <sub>1/3</sub> Mn <sub>1/3</sub> O <sub>2</sub> [30]	199.0	0.25
LaNiO <sub>3</sub> [31]	299.2	0.27
Nb:SrTiO <sub>3</sub> [32]	272.0	0.24

EDX detector at beam energy of 30 keV. Material maps of the region of interest (ROI) were thus acquired by counting the emitted X-Ray photons with material-characteristic wavelength.

#### 2.4. Electron nano-diffraction

To map the lattice parameter distribution within the NMC layer in its uncharged reference state, electron nano-diffraction was carried out using the JEOL ARM200CF high resolution STEM at a beam energy of 200 keV in nanobeam electron diffraction mode. Diffraction patterns were acquired using a high speed Gatan OneView Camera. Lattice rotation mapping and lattice strain calculations were carried out using the Gatan GMS3 software package [20].

Nano-diffraction peak identification was realised using a forward simulation approach: by simulating the diffraction pattern of an R3m LiNi<sub>1/3</sub>Co<sub>1/3</sub>Mn<sub>1/3</sub>O<sub>2</sub> unit cell using the CrystalMaker software suite [21], an exact match with the experimental pattern was achieved, thus providing full peak identification and a-axis lattice parameter information.

#### 2.5. FIB-DIC residual stress depth profiling

The FIB-DIC ring-core method is a well-established and thoroughly verified method for the semi-destructive probing of residual stresses at the micron scale [22]. It is based on the gradual removal of material in a ring-core shape with the intermediate acquisition of SEM frames at each milling steps. Mechanically disconnecting the central material 'island' from the surrounding strain field leads to a full elastic strain relief. This can be observed by tracking surface points of the central island using DIC in post-processing at an accuracy of around  $\varepsilon \approx 10^{-5}$ , which can then be used to back-calculate the average residual stresses present in the probed volume prior to milling, if the elastic properties of the material are known. Recent advances in this technique allow to extract the depth-dependant stress and strain profiles in milling direction, based on the FIB-DIC strain relief profiles and by employing the eigenstrain theory [23]. Material elastic constants used for the conversion of strain into stress are presented in Table 1.

### 3. Results and discussion

#### 3.1. Compressive residual stress in the as-deposited state

Compositional characterization of the epitaxially grown nanomultilayer battery was carried out using transmission Energy-Dispersive X-Ray Spectroscopy (t-EDX) on a thin, electron transparent lamella sectioned and polished using Focused Ion Beam (FIB). With the exception of Li that cannot be detected due to the very low characteristic X-Ray energy, the predominantly uniform distribution of other constituent elements was confirmed within the 50 nm thin LiNi<sub>1/3</sub>Co<sub>1/3</sub>Mn<sub>1/3</sub>O<sub>2</sub> (NMC111) cathode layer lying underneath the 500 nm thick Li<sub>3</sub>PO<sub>4</sub> solid electrolyte layer. Further details of the employed experimental techniques are provided in the 'Methods' section. The surface layer was a 1 µm thick metallic

Li anode film, as revealed by Scanning Transmission Electron Microscopy (STEM) imaging. A schematic overview of the sample is shown in Fig. 4a, alongside selected cross-sectional t-EDX material maps of the lamella indicated in Fig. 4b.

Leveraging the nano-resolution capabilities of the FIB-DIC ring-core method, residual stress depth profiles of the multilayer battery in the as-deposited state were obtained. For this purpose, four micro ring-cores with diameters of 10 µm and 5 µm were milled into the multilayer in a step-wise manner, as shown in the micrograph in Fig. 5. Before milling and in between milling steps, SEM frames were acquired which were subsequently employed for strain reconstruction using Digital Image Correlation (DIC). This well-established stress determination technique has been described in the past [22,33] and was found to provide a depth resolution of around 50 nm. Further details are provided in the 'Methods' section. The obtained x- and y-stress components are shown in Fig. 5. While the out-of-plane stress component  $\sigma_{zz}$  can be assumed to be zero in all layers due to the proximity to a free surface, pronounced compressive residuals stresses of up to 1 GPa were found in most of the individual layers, with peak compressive stress found in the NMC111 cathode and the LaNiO<sub>3</sub> electrode. Higher compression was observed across the y-component as compared to the x-component, which is likely related to growth mechanisms of the (104) oriented NMC layer. It should be noted that the extremely low mechanical stiffness of the Li surface layer is reflected in the near zero stress value. Further to the above, it can be seen that the boundary layer within the substrate mediating between highly compressive NMC layer and the stress-free far-field within the substrate is roughly equal in thickness to the total multilayer thickness.

While the respective crystallographic layer orientation was confirmed by XRD analysis in a previous study [17], further insights into the local microstructural properties within the (104) oriented NMC111 cathode were obtained from cross-sectional electron nano-diffraction mapping of the STEM lamella at beam energy of 200 keV within the Region of Interest (ROI) highlighted in Fig. 4b. A selected indexed electron nano-diffraction pattern is shown in Fig. 6a. For the peak identification and related lattice parameter determination, a forward simulation approach was chosen by simulating the R3m LiNi<sub>1/3</sub>Co<sub>1/3</sub>Mn<sub>1/3</sub>O<sub>2</sub> unit cell and finding the orientation that matched the observed diffraction pattern. Diffraction simulation along the [001] zone axis resulted in a diffraction pattern matching the Fig. 6a, thus providing peak identification for all diffraction peaks. An illustration of the NMC111 unit cell is shown in Fig. 6b.

Based on the cross-sectional cathode nano-diffraction maps, the local unit cell rotation around the [001] direction was determined with regard to the layer average pattern. While the STEM overview frame in Fig. 4 shows a uniform cathode layer microstructure without distinct features, the misorientation map in Fig. 7a reveals the presence of grains of a width comparable to the layer thickness. Low angle grain boundaries with lattice rotations of around  $\pm 5^\circ$  can be clearly identified and are highlighted in red. This finding has interesting implications for the lithiation and de-lithiation behavior during charge and discharge of the battery. Based on the assumption of uniform lithium migration across the entire cathode-electrolyte interface, a significant reduction in the interface resistance between (001) and (104)-oriented NMC111 film orientation was confirmed in a previous study [17]. In fact, small differences in grain orientation at grain boundaries (GB) may distort significantly the local lithium exchange dynamics and result in a slight reduction in the attainable charge rate in comparison to a highly ordered single crystalline layer.

In a further investigation, the nominal a-axis strain distribution at the grain level based on the layer average a-axis lattice parameter of 2.9 Å was calculated for a line profile crossing two grains,

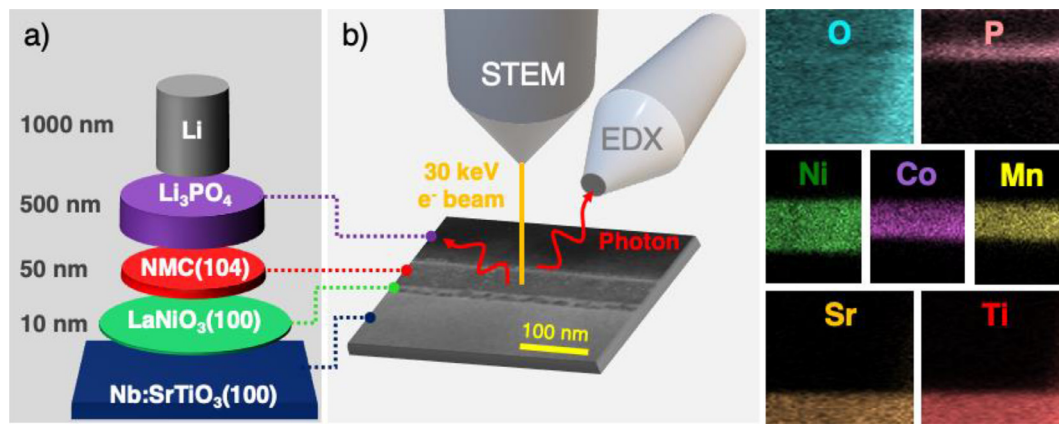


**Fig. 4.** t-EDX layer characterization for layer identification. a. Illustration of the individual layers composing the thin film battery. b. Selected overview of specific elemental t-EDX intensity maps color-coded by material, showing clear layer separation.

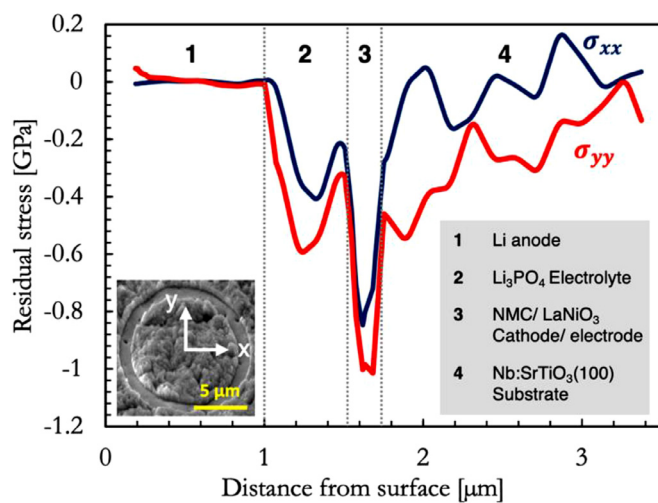


**Fig. 5.** Residual stress depth profile obtained from depth-resolved FIB-DIC analysis with individual layer identification. Bottom left: 10  $\mu\text{m}$  diameter FIB-DIC ring-core in the early stages of milling.

as shown in Fig. 7b. Clear differences between the lattice parameter values within the grain and at the boundary are visible that may be associated with intragranular variation in lithiation state of the pristine battery. As  $\text{Li}^+$  intercalation in NMC111 materials is associated with c-axis contraction and inelastic a-axis expansion

[34], the grain material can be assumed to be fully lithiated, as opposed to the grain boundary, which appears to be partly delithiated. Strain differences of up to 1.5% between grain and GB were found. Based on previously obtained *operando* lattice parameter data for NMC cathode material [11], it can be estimated that the a-axis lattice expansion of 1% is caused by a 1.6% c-axis contraction.

### 3.2. Strain evolution during in situ lamella charging

To obtain experimental insights into the de-lithiation induced cathode deformation, a  $10 \times 7 \times 1 \mu\text{m}^3$  lamella sample was extracted from the multilayer battery by FIB milling and polishing. A slot was created using FIB to prevent short circuit currents between anode and cathode as shown by the red arrow in Fig. 8a. The cathode current collector layer was attached to a TEM copper grid using the Pt deposition system, which was connected to the electrode of a pico-amp potentiostat. Subsequently, the W nanomanipulator needle was connected as counter electrode to the Pt surface layer deposited on top of the Li anode, as shown in Fig. 8a. As a result, a fully functioning micro-battery was electrically connected to a pico-ampere potentiostat that was integrated into the FIB-SEM instrument. As the sample was particularly beam sensitive, only very few images were acquired during sample preparation and mounting at low resolution, while only one high resolution SEM image was acquired before and after charging, respectively. While this procedure prevented the time-resolved *operando*

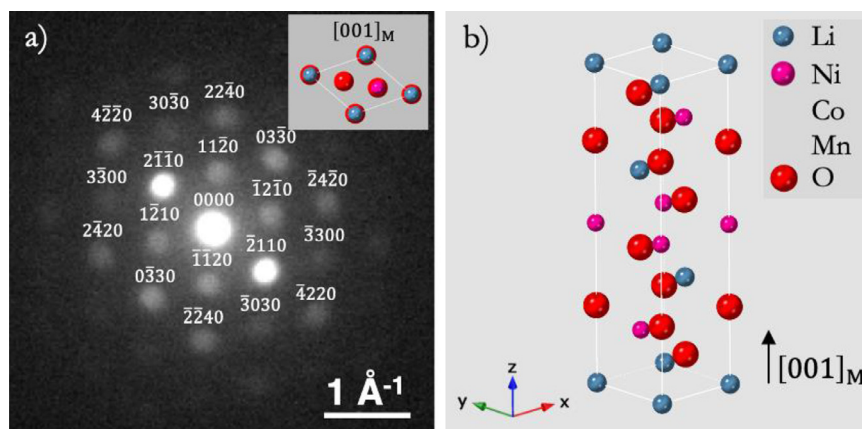


**Fig. 6.** Electron nano-diffraction for grain orientation analysis. a. Nano-diffraction pattern obtained from TEM with identified peaks based on  $R\bar{3}m$  unit cell along the  $[001]$  zone axis, as indicated in the top right corner. b. Illustration of NMC  $R\bar{3}m$  unit cell.

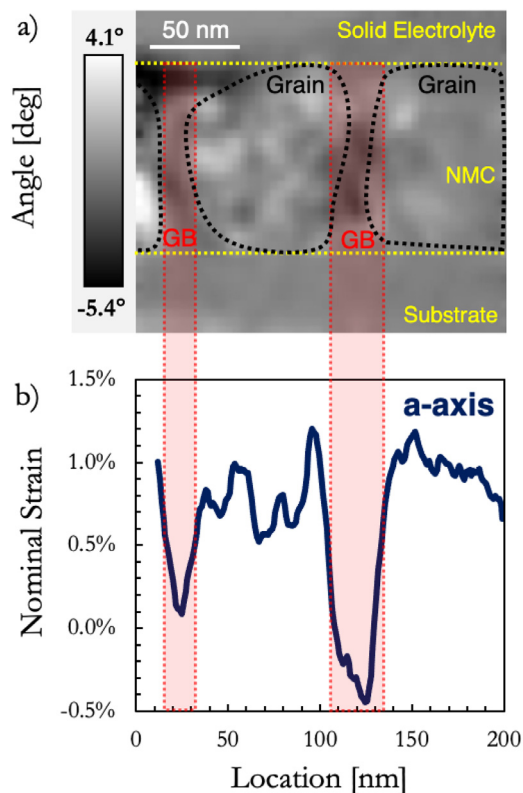


**Fig. 7a.** Misorientation angle within NMC layer with respect to layer average clearly revealing low angle grain boundaries highlighted in red. Individual NMC grains are highlighted by black dashed line. b. Line average of nominal elastic a-axis strain across two grains shown in a) with respect to layer average value highlighting strain gradients between grains and grain boundaries in the as-deposited state.

analysis of strains, it enabled a comparison of the horizontal and vertical cathode strain before and after de-lithiation. The built-in potentiostat could only be operated in potentiostatic mode by prescribing a voltage ramp. A voltage ramp from 2 V to 4.5 V was programmed for a duration of 120 s, during which the current was recorded as shown in the graph in Fig. 8a and after which the voltage was held at 5 V.

Digital Image Correlation (DIC) software [19] was subsequently employed to track surface contrast features arising from FIB polishing, also known as ‘FIB curtaining’, which can be seen as vertical lines in the micrographs shown in Fig. 8b, c. The horizontal

and vertical strain components obtained from DIC analysis were  $\varepsilon_{xx} = 0.22 \pm 0.03\%$  and  $\varepsilon_{zz} = 2.35 \pm 0.18\%$ , respectively, while the shear strain component was determined as  $\varepsilon_{xz} = -2.69 \pm 0.21\%$ . Based on this data, principal strains were determined as  $\varepsilon_1 = 4.18\%$  and  $\varepsilon_2 = -1.61\%$ , with a principal angle  $\theta_p = 55.8^\circ$ . These results not only match the expected  $\text{Li}^+$  diffusion direction of the (104) oriented cathode grains, but also indicate a significant c-axis expansion perpendicular to and a-axis contraction in the direction of the  $\text{Li}^+$  diffusion upon de-lithiation. These results are summarised in Fig. 9.

While the multilayer expansion is not constrained in the vertical direction, horizontal displacement and thus strain is hindered by the interlayer adhesion between solid electrolyte, cathode, and current collector. A free-standing, unconstrained NMC111 (104) layer would expand nearly equibiaxially in x- and y- direction. The presence of constraint resulted in the expansion in horizontal direction being hindered, giving rise to stress. Based on this assumption and using typical stiffness values for the material, the de-lithiation induced stress can be quantified at a level of around  $-4$  GPa compression. As a result, stress interaction between the compressed NMC111 layer and the surrounding layers leads to tensile residual stress being introduced in the neighbouring layers and particularly in the vicinity of layer interfaces. Given the previously identified high quality of the cathode-electrolyte interface [13], it is not surprising that this interface is able to withstand the stress transfer. Instead, the weakest mechanical link appears to be the Lithium-electrolyte interface, which shows signs of degradation after a single charge. Indicators confirming this assumption were observed in form of newly formed voids at the Lithium-solid electrolyte interface, as can be seen by comparing Fig. 8b and c, which show the micro-battery before and after charge, respectively. While a minor void identified before the first charge might have been caused by a sudden change in voltage due to the connection of the electrodes to the potentiostat, a clear increase in pre-existing void size should be noted, along with a newly formed crack. The location and shape of the newly formed crack support the hypothesis of strain-induced damage caused by cathode expansion during lithium de-intercalation upon charge. The large expansion in the vertical direction further aligns with literature data on the c-axis lattice parameter strain during charge [34]. It can be hypothesised that the observed void formation results in an increase in the interfacial resistance, which is consistent with the response observed during previous experiments [17]. The largest drop in charging current was observed between the first and second charge cycle, which aligns well with the observed mechanical degradation: after the initial crack and void formation, expansion and contraction of

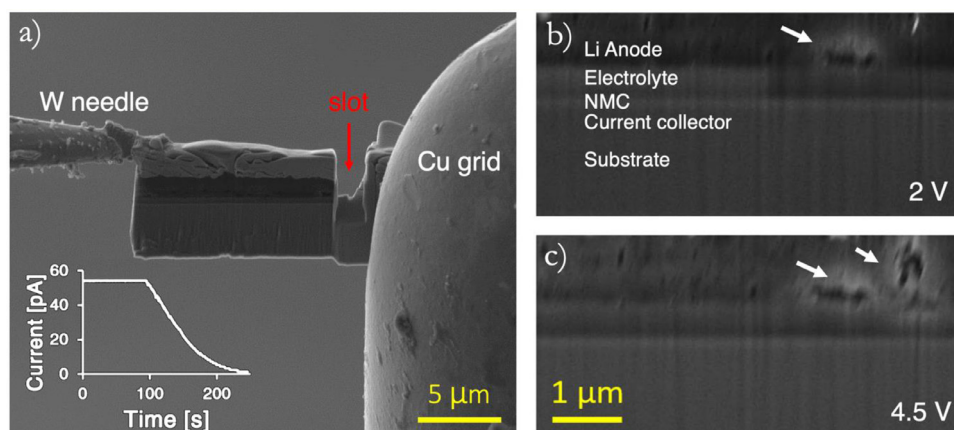


**Fig. 8.** In situ lamella charging. a. SEM micrograph of the lamella battery with electric connection acquired after the charging experiment due to sample beam sensitivity. Bottom left: charging current versus time following voltage ramp. b. SEM micrograph of the lamella battery before and c. after charge.



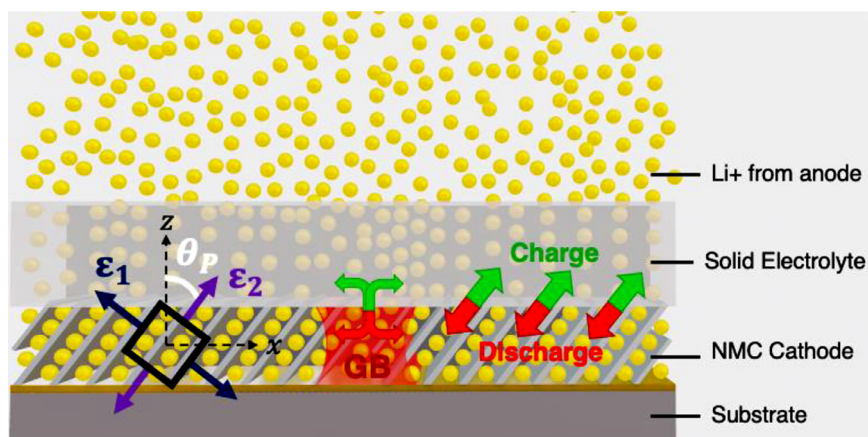


Fig. 9. Illustration of the interaction between lithium migration, strain and microstructure. Principal strains and principal angle are illustrated on the left.

the cathode layer in subsequent cycles does not induce further microstructural damage of comparable magnitude, since the material has been permanently modified by plastic deformation and voiding, leading to improved accommodation and a reduction in stiffness.

#### 4. Modeling and simulation

To enable a time resolved understanding of the strain and stress build-up in thin film batteries during de-lithiation upon charge, a coupled diffusion-strain simulation was implemented in COMSOL Multiphysics®, which combined the solution of a generalised diffusion equation with sequentially coupled strain and stress analysis. More precisely, the model consisted of solving the diffusion equation for a Li-concentration gradient within the NMC111 layer using a prescribed boundary concentration. In a second step, the calculated concentration was related to strain in prescribed expansion directions based on the known crystallographic (104) orientation, and finally converted into stress. To quantify the effect of a grain orientation change in the NMC layer on the arising stress fields, a (100) oriented NMC layer was simulated for comparison. A lithium concentration of 20% was assumed for the fully charged cathode, while a lithium saturation of 100% was assumed for the fully discharged state. The material parameters used are listed in Table 1 in the 'Methods' section.

Fig. 10 shows the Li distribution within the cathode, as well as the horizontal stress and vertical strain for both (104) and (001) oriented cathode material. It can be seen that for a single charge simulated at a charge rate 3600C, cathode de-lithiation duration of 0.5 s was obtained. Experiments at of 14 mAcm<sup>-2</sup> (3600C) have been conducted on the present samples in previous studies [13] and are of particular interest for the study of microstructural strain and degradation, due to the resulting high stress and strain gradients, which have been quantified in this simulation. As the lithium diffusion mechanism through direct intercalation in (104) oriented cathode material versus GB dominated horizontal diffusion in (001) oriented NMC111 was not accounted for in the present model, identical de-lithiation curves can be seen in Fig. 10a, b. When looking at the resulting horizontal stress, however, large differences in stress accommodation can be observed between the two analysed microstructures. (104) oriented material expands in c-axis direction during charge, resulting in equal horizontal and vertical expansion. Due to the multilayer constraint, free expansion is only possible in the vertical direction, resulting in a strain of around 1.5%, as shown in Fig. 10f. The location of the cathode is shaded red. The horizontal strain com-

ponent, however, is hindered by interface cohesion and results in an in-plane horizontal compressive stress of around -3 GPa, as can be seen in Fig. 10d. Balancing tensile residual stresses in the adjacent layers reach values of up to around 0.4 GPa, which can be detrimental for the structural integrity of nanostructured coatings.

Significantly different results were obtained for (100) oriented material, as the de-lithiation resulted in vertical expansion of the c-axis and horizontal contraction of the a-axis. Simulated horizontal stresses were therefore tensile, reaching values of up to 0.8 GPa as shown in Fig. 10c. The unconstrained vertical strain reached around 2.2% as can be seen in Fig. 10e. Overall, the simulation results indicated large in-plane tensile stresses for (001) oriented NMC111 cathodes, while highly compressive stresses were identified in (104) oriented cathodes.

Combining electron nano-diffraction, FIB-DIC depth profiling and *in situ* lamella charging with DIC and multiphysics modeling clearly demonstrated that the choice of grain orientation in thin film cathodes has fundamental implications for the strain fields and degradation that unfurl in the entire solid state battery upon charging. Electron nano-diffraction revealed the strain accommodation mechanisms in the as-deposited samples with large strain variations between grains and grain boundaries, in which the grain boundaries act as strain buffers accommodating the lithium-induced a-axis lattice expansion. FIB-DIC depth profiling further showed that the as-deposited samples are under large compressive stresses, thus confirming the local nano-diffraction observations. *In situ* lamella charging in combination with DIC helped quantifying the horizontal and vertical strain within the NMC111 layer, which showed a significant expansion in the vertical direction and stress build-up in the horizontal direction.

The observed interface crack and void growth further supported the described mechanism as a significant driver underlying the increase of the Lithium-electrolyte interfacial resistance between the first and second charge cycle. The formation mechanism of these defects was identified as stress accommodation by the Lithium anode, resulting in horizontal tensile strain build-up and micro-scale fracture. Multiphysics simulation of the de-lithiation process further confirmed the experimental observation and showed close agreement with the experimental observations. Based on the findings described in the present work, a (104) NMC111 grain orientation appears more favourable both for moderating the interfacial resistance and due to the lack of tensile stress which was found to arise in (001)-oriented cathode material.

To prevent crack growth at the anode-electrolyte interface, the compressive residual stress within the solid electrolyte or Lithium

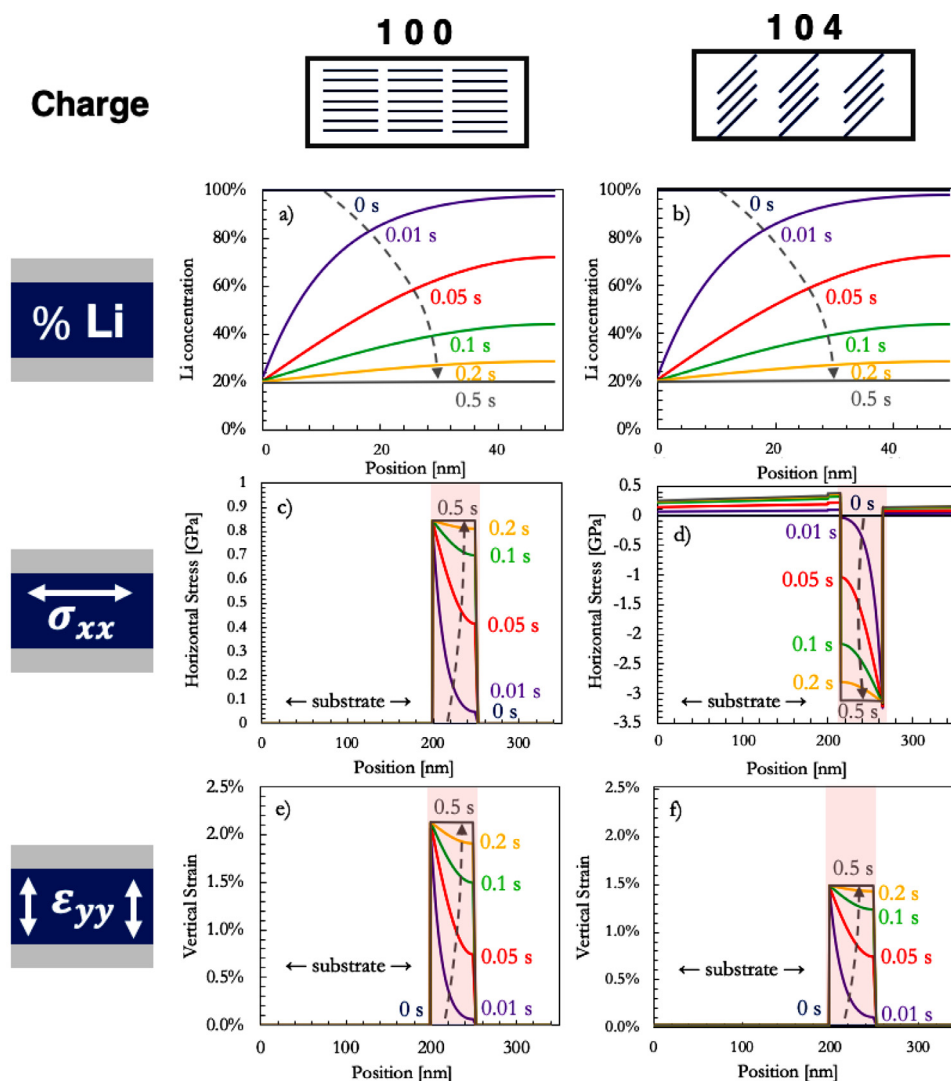


**Fig. 10.** a,b. COMSOL simulation results showing the lithiation state versus time within the NMC layer for the (100) and (104) oriented cathode. c,d. Horizontal stress within the NMC layer for (100) and (104) oriented cathode. e,f. Vertical strain within the NMC layer for (100) and (104) oriented cathode.

layer could be increased, therefore ensuring mechanical expansion and contraction within the elastic regime of the Lithium anode.

## 5. Conclusion

A novel experimental combination of *in situ* solid state battery lamella charging combined with Digital Image Correlation and electron nano-diffraction was used for the quantitative evaluation of strains arising within thin film batteries during charge and discharge. The obtained data was correlated with the as-deposited battery state and crystallographic orientation of the cathode, to develop in-depth understanding of the mechanisms leading to interface degradation and loss of capacity. By means of finite element simulation it was demonstrated that the horizontally constrained expansion of the (100) oriented cathode layer results in the formation of tensile stress within the cathode layer, giving rise to increased crack and void formation along the anode-electrolyte interface, while the (104) oriented cathode was shown to have superior charging rates and mechanical stability. This investigation demonstrates that the modification and control of the residual stress in the cathode layer can be used to mitigate the degradation upon

first charge, thus preventing significant loss of capacity that may reach up to 28%.

## Declaration of Competing Interest

There are no conflicts of interest to declare.

## CRediT authorship contribution statement

**León Romano Brandt:** Conceptualization, Methodology, Validation, Formal analysis, Investigation, Writing – original draft, Writing – review & editing, Visualization. **Kazunori Nishio:** Methodology, Investigation, Writing – review & editing. **Enrico Salvati:** Methodology, Formal analysis, Investigation, Writing – review & editing. **Kevin P. Simon:** Methodology, Resources, Writing – review & editing. **Chrysanthi Papadaki:** Methodology, Resources, Writing – review & editing. **Taro Hitosugi:** Conceptualization, Methodology, Data curation, Writing – review & editing, Supervision, Funding acquisition. **Alexander M. Korsunsky:** Conceptualization, Methodology, Writing – review & editing, Resources, Supervision, Project administration.



## Acknowledgements

The authors would like to acknowledge Diamond Light Source (Harwell, UK) for the allocation of beamtime under beam time numbers MG24560-1 and MG24560-2, as well as Dr Mohsen Danaie and Dr Christopher Allen for their support during the experimental sessions. We would further thank John-Joseph Marie (University of Oxford) for his experimental support. A.M.K. acknowledges funding received from the Engineering and Physical Sciences Research Council (EPSRC) [EP/P005381/1] and [EP/S005072/1].

## References

- [1] M. Dachyar, T.Y.M. Zagloel, L.R. Saragih, Knowledge growth and development: internet of things (IoT) research, 2006–2018, *Heliyon* 5 (2019) e02264, doi:[10.1016/j.heliyon.2019.e02264](https://doi.org/10.1016/j.heliyon.2019.e02264).
- [2] M. Sugiyama, T. Uemura, M. Kondo, M. Akiyama, N. Namba, S. Yoshimoto, Y. Noda, T. Araki, T. Sekitani, An ultraflexible organic differential amplifier for recording electrocardiograms, *Nat. Electron.* 2 (2019) 351–360, doi:[10.1038/s41528-019-0283-5](https://doi.org/10.1038/s41528-019-0283-5).
- [3] M. Zulqarnain, S. Stanzione, G. Rathinavel, S. Smout, M. Willegems, K. Myny, E. Cantatore, A flexible ECG patch compatible with NFC RF communication, *Npj Flex. Electron.* 4 (2020) 1–8, doi:[10.1038/s41528-020-0077-x](https://doi.org/10.1038/s41528-020-0077-x).
- [4] Y. Jin, G. Chen, K. Lao, S. Li, Y. Lu, Y. Gan, Z. Li, J. Hu, J. Huang, J. Wen, H. Deng, M. Yang, Z. Chen, X. Hu, B. Liang, J. Luo, Identifying human body states by using a flexible integrated sensor, *Npj Flex. Electron.* 4 (2020) 1–8, doi:[10.1038/s41528-020-00090-9](https://doi.org/10.1038/s41528-020-00090-9).
- [5] D. Ruzmetov, V.P. Oleshko, P.M. Haney, H.J. Lezec, K. Karki, K.H. Baloch, A.K. Agrawal, A.V. Davydov, S. Krylyuk, Y. Liu, J. Huang, M. Tanase, J. Cummings, A.A. Talin, Electrolyte stability determines scaling limits for solid-state 3D Li ion batteries, *Nano Lett* 12 (2012) 505–511, doi:[10.1021/nl204047z](https://doi.org/10.1021/nl204047z).
- [6] Y. Liu, Y. Zhu, Y. Cui, Challenges and opportunities towards fast-charging battery materials, *Nat. Energy* 4 (2019) 540–550, doi:[10.1038/s41560-019-0405-3](https://doi.org/10.1038/s41560-019-0405-3).
- [7] A. Tomaszewska, Z. Chu, X. Feng, S. O'Kane, X. Liu, J. Chen, C. Ji, E. Endler, R. Li, L. Liu, Y. Li, S. Zheng, S. Vetterlein, M. Gao, J. Du, M. Parkes, M. Ouyang, M. Marinescu, G. Offer, B. Wu, Lithium-ion battery fast charging: a review, *ETransportation* 1 (2019) 100011, doi:[10.1016/j.etrans.2019.100011](https://doi.org/10.1016/j.etrans.2019.100011).
- [8] E. Quartarone, P. Mustarelli, Review—emerging trends in the design of electrolytes for lithium and post-lithium batteries, *J. Electrochem. Soc.* 167 (2020) 050508, doi:[10.1149/1945-7111/ab63c4](https://doi.org/10.1149/1945-7111/ab63c4).
- [9] R. Schmich, R. Wagner, G. Hörpel, T. Placke, M. Winter, Performance and cost of materials for lithium-based rechargeable automotive batteries, *Nat. Energy* 3 (2018) 267–278, doi:[10.1038/s41560-018-0107-2](https://doi.org/10.1038/s41560-018-0107-2).
- [10] R. Chen, T. Zhao, X. Zhang, L. Li, F. Wu, Advanced cathode materials for lithium-ion batteries using nanoarchitectonics, *Nanoscale Horizons* 1 (2016) 423–444, doi:[10.1039/c6nh00016a](https://doi.org/10.1039/c6nh00016a).
- [11] L.R. Brandt, J.-J. Marie, T. Moxham, D.P. Förstermann, E. Salvati, C. Besnard, C. Papadaki, Z. Wang, P.G. Bruce, A.M. Korsunsky, Synchrotron X-ray quantitative evaluation of transient deformation and damage phenomena in a single nickel-rich cathode particle, *Energy Environ. Sci.* (2020) 3556–3566, doi:[10.1039/d0ee02290j](https://doi.org/10.1039/d0ee02290j).
- [12] U.H. Kim, G.T. Park, B.K. Son, G.W. Nam, J. Liu, L.Y. Kuo, P. Kaghazchi, C.S. Yoon, Y.K. Sun, Heuristic solution for achieving long-term cycle stability for Ni-rich layered cathodes at full depth of discharge, *Nat. Energy* 5 (2020) 860–869, doi:[10.1038/s41560-020-00693-6](https://doi.org/10.1038/s41560-020-00693-6).
- [13] H. Kawasoko, S. Shiraki, T. Suzuki, R. Shimizu, T. Hitosugi, Extremely low resistance of Li<sub>3</sub>PO<sub>4</sub> electrolyte/Li(Ni<sub>0.5</sub>Mn<sub>1.5</sub>)O<sub>4</sub> electrode interfaces, *ACS Appl. Mater. Interfaces* 10 (2018) 27498–27502, doi:[10.1021/acsami.8b08506](https://doi.org/10.1021/acsami.8b08506).
- [14] J. Wu, L. Shen, Z. Zhang, G. Liu, Z. Wang, D. Zhou, H. Wan, X. Xu, X. Yao, All-solid-state lithium batteries with sulfide electrolytes and oxide cathodes, *Electrochem. Energy Rev.* 41 (4) (2020) 101–135 (2020), doi:[10.1007/s41918-020-00081-4](https://doi.org/10.1007/s41918-020-00081-4).
- [15] J. Wu, S. Liu, F. Han, X. Yao, C. Wang, Lithium/sulfide all-solid-state batteries using sulfide electrolytes, *Adv. Mater.* 33 (2021) 2000751, doi:[10.1002/adma.202000751](https://doi.org/10.1002/adma.202000751).
- [16] Q. Zhao, S. Stalin, C.Z. Zhao, L.A. Archer, Designing solid-state electrolytes for safe, energy-dense batteries, *Nat. Rev. Mater.* 5 (2020) 229–252, doi:[10.1038/s41578-019-0165-5](https://doi.org/10.1038/s41578-019-0165-5).
- [17] K. Nishio, N. Nakamura, K. Horiba, M. Kitamura, H. Kumigashira, R. Shimizu, T. Hitosugi, Impact of the Crystal Orientation of Positive Electrodes on the Interface Resistance across a Solid Electrolyte and Electrode, *ACS Appl. Energy Mater.* 3 (2020) 6416–6421, doi:[10.1021/acsaelm.0c00644](https://doi.org/10.1021/acsaelm.0c00644).
- [18] K. Simon, L. Porz, T. Swamy, Y.M. Chiang, A. Slocum, Low-profile self-sealing sample transfer flexure box, *Rev. Sci. Instrum.* 88 (2017), doi:[10.1063/1.4997952](https://doi.org/10.1063/1.4997952).
- [19] C. Eberl, Digital Image Correlation and Tracking, MATLAB Cent. File Exch. (2020). <https://www.mathworks.com/matlabcentral/fileexchange/12413-digital-image-correlation-and-tracking> (accessed July 22, 2020).
- [20] Gatan Microscopy Suite Software | Gatan, Inc., (n.d.). <https://www.gatan.com/products/tem-analysis/gatan-microscopy-suite-software> (accessed November 23, 2020).
- [21] CrystalMaker: Overview, (n.d.). <http://crystallmaker.com/crystallmaker/index.html> (accessed November 23, 2020).
- [22] L. Romano-Brandt, E. Salvati, E. Le Bourhis, T. Moxham, I.P. Dolbnya, A.M. Korsunsky, Nano-scale residual stress depth profiling in Cu/W nano-multilayers as a function of magnetron sputtering pressure, *Surf. Coatings Technol.* 381 (2020) 125142, doi:[10.1016/j.surfcoat.2019.125142](https://doi.org/10.1016/j.surfcoat.2019.125142).
- [23] A.M. Korsunsky, A Teaching Essay On Residual Stresses and Eigenstrains, Butterworth-Heinemann, 2017.
- [24] A.M. James, MacMillan's chemical and physical data, *Biochem. Educ.* 21 (1993) 109–110, doi:[10.1016/0307-4412\(93\)90067-a](https://doi.org/10.1016/0307-4412(93)90067-a).
- [25] O.S. Bondareva, M.A. Simonov, N.V. Belov, The crystal structure of the synthetic analogue of the lithiophosphate Li<sub>3</sub>PO<sub>4</sub> -gamma, *Dokl. Akad. Nauk SSSR* 240 (1978) 75–77.
- [26] W.H. Baur, Solid solutions between octahedral and tetrahedral olivine types in Li-Zn-germanates, *Inorg. Nucl. Chem. Lett.* 16 (1980) 525–527.
- [27] B. Wang, B.C. Chakoumakos, B.C. Sales, B.S. Kwak, J.B. Bates, Synthesis, crystal structure, and ionic conductivity of a polycrystalline lithium phosphorus oxynitride with the gamma-Li<sub>3</sub>P O<sub>4</sub> structure, *J. Solid State Chem.* 115 (1995) 313–323.
- [28] O.V. Yakubovich, V.S. Urusov, Electron distribution in lithiophosphatite: crystallochemical features of orthophosphates with hexagonal close packing, *Kristallografiya* 42 (1997) 301–308.
- [29] J. Zemann, Die Kristallstruktur von Lithiumphosphat, Li<sub>3</sub>P O<sub>4</sub>, *Acta Crystallogr* 13 (1960) 863–867.
- [30] E.J. Cheng, K. Hong, N.J. Taylor, H. Choe, J. Wolfenstine, J. Sakamoto, Mechanical and physical properties of LiNi<sub>0.33</sub>Mn<sub>0.33</sub>Co<sub>0.33</sub>O<sub>2</sub> (NMC), *J. Eur. Ceram. Soc.* 37 (2017) 3213–3217, doi:[10.1016/j.jeurceramsoc.2017.03.048](https://doi.org/10.1016/j.jeurceramsoc.2017.03.048).
- [31] V.J. Masys, Elastic properties of rhombohedral, cubic, and monoclinic phases of LaNiO<sub>3</sub> by first principles calculations, *Comput. Mater. Sci.* 108 (2015) 153–159, doi:[10.1016/j.commatsci.2015.06.034](https://doi.org/10.1016/j.commatsci.2015.06.034).
- [32] mp-5229: SrTiO<sub>3</sub> (cubic, Pm-3m, 221), (n.d.). <https://www.materialsproject.org/materials/mp-5229/> (accessed November 28, 2020).
- [33] E. Salvati, L. Romano-Brandt, M.Z. Mughal, M. Sebastiani, A.M. Korsunsky, Generalised residual stress depth profiling at the nanoscale using focused ion beam milling, *J. Mech. Phys. Solids* (2019), doi:[10.1016/j.jmps.2019.01.007](https://doi.org/10.1016/j.jmps.2019.01.007).
- [34] X.L. Wang, K. An, L. Cai, Z. Feng, S.E. Nagler, C. Daniel, K.J. Rhodes, A.D. Stoica, H.D. Skorpenske, C. Liang, W. Zhang, J. Kim, Y. Qi, S.J. Harris, Visualizing the chemistry and structure dynamics in lithium-ion batteries by in-situ neutron diffraction, *Sci. Rep.* 2 (2012) 1–7, doi:[10.1038/srep00747](https://doi.org/10.1038/srep00747).